ChemElectroChem

Research Article
doi.org/10.1002/celc.202400151

Chemistry Europe
European Chemical Societies Publishing

www.chemelectrochem.org

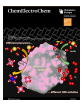

Effect of the Precursor Metal Salt on the Oxygen Evolution Reaction for NiFe Oxide Materials

Axel Zuber,*[a] Ilias M. Oikonomou,[b, c] Lee Gannon,[c, d] Igor Chunin,[c, d] Lukas Reith,[e] Belin Can,[a] Mailis Lounasvuori,[g] Thorsten Schultz,[h, i] Norbert Koch,[h, i] Cormac McGuinness,[c, d] Prashanth W. Menezes,[e, f] Valeria Nicolosi,[b, c] and Michelle P. Browne*[a]

Bimetallic nickel-iron based oxides are regarded as one of the most promising catalysts for the oxygen evolution reaction (OER). In this study, we show that the precursor metal salts can affect the OER activity of the resulting Ni/Fe oxide under the same hydrothermal synthesis conditions. Pure sulfate, pure nitrate and mixed sulfate/nitrate metal salts were used to fabricate NiFe based oxide materials and to study the importance of the precursor choice for the OER. The results show that the nature of the precursor used in the synthesis of the bimetallic nickel-iron materials can influence different multi-phase catalysts to form which effects the OER.

[a] *Dr. A. Zuber, B. Can, Dr. M. P. Browne*
Helmholtz Young Investigator Group Electrocatalysis: Synthesis to Devices
Helmholtz-Zentrum Berlin für Materialien und Energie
Hahn-Meitner-Platz 1, 14109, Berlin, Germany
E-mail: axel.zuber@helmholtz-berlin.de
michelle.browne@helmholtz-berlin.de

[b] *I. M. Oikonomou, Prof. V. Nicolosi*
School of Chemistry
Trinity College Dublin
College Green, Dublin 2, Ireland

[c] *I. M. Oikonomou, L. Gannon, I. Chunin, Dr. C. McGuinness, Prof. V. Nicolosi*
CRANN and AMBER Research Centres
Trinity College Dublin
College Green, Dublin 2, Ireland

[d] *L. Gannon, I. Chunin, Dr. C. McGuinness*
School of Physics
Trinity College Dublin
College Green, Dublin 2, Ireland

[e] *Dr. L. Reith, Dr. P. W. Menezes*
Department of Chemistry, Metalorganics, and Inorganic Materials
Technische Universität Berlin
Straße des 17 Juni 135, Sekr. C2, 10623 Berlin, Germany

[f] *Dr. P. W. Menezes*
Materials Chemistry Group for Thin Film Catalysis – CatLab
Helmholtz-Zentrum Berlin für Materialien und Energie
Albert-Einstein-Str. 15, 12489 Berlin, Germany

[g] *Dr. M. Lounasvuori*
Nanoscale Solid-Liquid Interfaces
Helmholtz-Zentrum Berlin für Materialien und Energie GmbH
Albert-Einstein-Str. 15, 12489 Berlin, Germany

[h] *Dr. T. Schultz, Dr. N. Koch*
Helmholtz-Zentrum Berlin für Materialien und Energie GmbH
Berlin, 14109, Germany

[i] *Dr. T. Schultz, Dr. N. Koch*
Institut für Physik & IRIS Adlershof
Humboldt-Universität zu Berlin
Berlin, 12489, Germany

Supporting information for this article is available on the WWW under https://doi.org/10.1002/celc.202400151

Introduction

According to the latest Intergovernmental Panel on Climate Change report, global temperature is likely to increase by 4 °C over the next years.[1] Green hydrogen (H_2) is at the center of the future leading technologies to hinder this catastrophic event from happening. Green H_2 is produced by electrochemical water splitting.[2] Water splitting consists of simultaneous oxidation and reduction of water by electrochemical processes, denoted as the oxygen evolution reaction (OER) and the hydrogen evolution reaction (HER), respectively.

Even though the goal of water splitting is to produce green H_2 on the cathode, it is the opposite reaction, the OER, that is the bottleneck of water splitting due to the large overpotential (η). Hence, the OER overpotential must be decreased for efficient H_2 production to take place by catalysts that can achieve this. Additionally, the target catalyst should be abundant, cost-efficient, environmentally friendly, and stabile in electrolyzers for years if not for decades.[3] First-row transition metal oxides (TMOs), largely based on cobalt, manganese, nickel, and iron, have long been targeted as optimum OER catalyst for alkaline based electrolysis.[4]

It is well known that nickel and cobalt oxide/hydroxide pre-catalyst are known to undergo changes in surface chemistry under potential and reach high oxidation states (IIàIIIàIV transitions) which are thought to be the active intermediates/sites for the OER.[5] Manganese and iron are attractive for their abundance, but their poor intrinsic activity towards OER has prompted researchers to combine them with different materials to develop cheap and highly active materials.[5c,6] In recent years, the role of iron in enhancing the intrinsic activity of the nickel-based materials, since its first discovery by Corrigan *et al.* in the 1970s, has re-surfaced.[7] In the last decade, a significant number of studies have been dedicated to nickel-iron layered double hydroxide (NiFe LDH) or iron incorporated nickel compounds[8] for the OER. However, despite their good activity,

NiFe based materials exhibit low conductivity and exhibit stability issues.[9]

NiFe based materials for OER are routinely synthesized by a large variety of methods such as co-precipitation,[8e,10] electrodeposition,[11] template-assisted methods,[12] and hydrothermal/solvothermal synthesis.[5a,11b,13] Interestingly, the hydrothermal/solvothermal synthesis of nickel-iron based materials in literature significantly varies in terms of the reactants and synthesis parameters which also leads to a variation in OER performances, as summarized in Table 1.

For the hydrothermal/solvothermal synthesis, the common reaction media used include urea, dimethylformamide (DMF) and ethylene glycol (EG),while the metal salts are typically nitrate, sulfate, acetylacetonate or acetate. The hydrothermal treatment temperatures and durations of the synthesis range from 90 to 205 °C and 15 mins to 2 days, respectively. Most of the synthesis procedures use additives to tune the crystals shape and interlayer spacing (triethanolamine, sodium dodecyl sulfonate (SDS), ammonium salts) or incorporate a support material (e.g. nickel foam (NF), graphite foils, carbon paper) into the reaction vessel for the NiFe materials to be directly deposited onto the support. Regarding performance for OER, the resulting materials vary, with overpotentials at a current density of 10 mA cm^{-2} ranging from 170–360 mV and Tafel slope between 30–60 mV/dec, Table 1.

One can note that there is a wide range of metal salt precursors used in the fabrication of the NiFe materials. However, studies justifying the preferential use of a precursor over another for NiFe based materials for the OER is lacking in the literature. Yet, the importance of the precursor salt for other materials and/or for other applications have been highlighted by several studies.[16] For example, Zharan and colleagues showed how the deposition using four different anion salts (SO_4^{2-}, NO_3^-, Cl^-, and Ac), can change the oxidation state of the nickel oxide formed and affect the resulting film crystallinity thus, resulting in various OER activities for the nickel oxides.[16d] Similarly, Petrucci *et al.* demonstrated how the combination of different metal salts can make electrodeposited ruthenium-manganese films more capacitive and susceptible to corrosion.[17] Sou and co-workers compared citrate, nitrate and acetate based zeolite-supported nickel catalysts for carbon oxide methanation, showing that the choice of precursor influences the metal impregnation of the metal on a support.[16a] Hence, understanding how to manipulate the OER activity of NiFe based materials by simply modifying metal salt precursors is a simple route to promote materials discovery for this oxidative reaction.

In this paper, we show the importance of using a single or mixed metal salt precursors based on sulfates and nitrates in a simple urea-assisted hydrothermal synthesis of NiFe based materials for the OER. We show how the by-products induced by the choice of the metal precursor can affect the formation of the targeted NiFe material during a simple hydrothermal process and the fluctuation of their behavior under OER potentials.

Results and Discussion

Urea-Assisted Synthesis of the Compounds

To fabricate the NiFe based materials, a urea-assisted hydrothermal synthesis method was used, and the metal salt precursors were varied to study the effect of the metal precursor salt on the OER, Figure 1. The nickel-iron oxide urea-assisted synthesis was carried out using a Ni:Fe = 1:1 molar ratio in urea and water then added to the hydrothermal vessel. The hydrothermal synthesis was carried at 120 °C for 12 h and the resulting powder was washed and dried. When the sulfate and nitrate precursor salts were each used separately to make the NiFe oxide, the material in this study will be denoted as 'SO_4 or sulfate material' and 'NO_3 or nitrate material', respectively. Furthermore, the NiFe oxide fabricated by the nickel

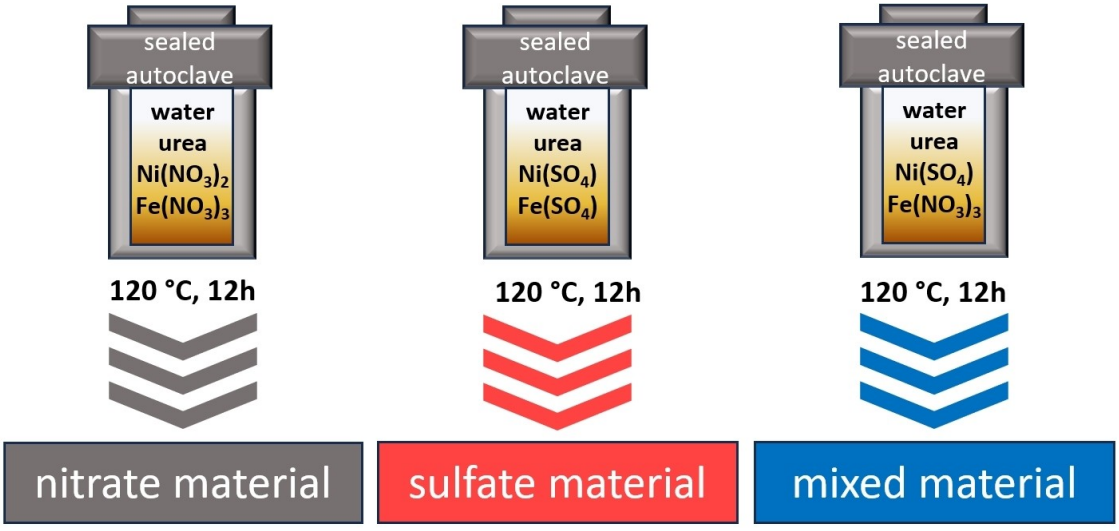

Figure 1. Schematic of synthetic procedure showing the nomenclature of the various NiFe catalysts in this study.

Table 1. Hydrothermal synthesis conditions and OER performance of nickel-iron based materials in literature.

Material [ref]	Medium Additive/support	Salts ratio (Ni:Fe)	T (°C)/time (h)	η (mV) Tafel slope (mV/dec)	ref electrode electrolyte mass loading (mg/cm^2)	Technical, economic, and social aspect notes related to synthesis procedure if applicable
NiFeO [13a]	urea (aq.) nickel foam (NF)	NO_3 3:1–1:3	160/16	$\eta_{10}=170$ 21	Ag/AgCl, 1 M KOH	Foam electrodes may cause inaccurate inherent catalytic performance estimations[14]
NiFe LDH/NGF [13b]	urea (aq.) N-doped graphite foils	SO_4 8:1	180/12	$\eta_{10}=233$ 59.4	Hg/HgO, 1 M KOH, 1.1	
NiFe-LDH/C [13c]	urea (aq) – L-ascorbic acid NF	NO_3 3:1	120/6	$\eta_{50}=234$ 56	Hg/HgO, 1 M KOH	
NiFe-LDH/C [15]	DMF MNBI	NO_3 2:1	160/12	$\eta_{10}=210$ 35	Ag/AgCl, 1 M KOH	DMF is not safe for women to use due to infertility links
$Ni_{0.45}Fe_{0.55}O_x$ [5a]	Benzenediol-benzyl alcohol –	NO_3: accac 1:1	190/0.25	– –	RHE 0.1 M KOH –	
Fe doped Ni oxide [13d]	tert-butanol –	Acac 4:1–20:1	205/20–30	$\eta_{10}=300$ –	Ag/AgCl 0.5 M KOH –	This synthesis method uses the highest temp and longest time (cost more electricity) but leads to a catalyst with lower OER activity than other studies in the table.
NiFe LDH [13e]	water-DMF –	OAc: NO_3 5:1	130/16 + 170/2	$\eta_{10}=360$ 51	RHE 0.1 KOH –	This synthesis requires two hydrothermal treatments to obtain the material
NiFe LDH/CNT [13f]	water-DMF –	OAc: NO_3 1:1	120/4 + 160/2	$\eta_{10}=220$ 31	Hg_2Cl_2 1 M KOH 0.2	This synthesis requires two hydrothermal treatments to obtain the material
NiFe LDH [13g]	urea (aq.) triethanolamine	NO_3 3:1	150/48	$\eta_{10}=300$ 40	Hg/HgO, 1 M KOH, 1	This synthesis uses the longest duration for the hydrothermal synthesis, which is more energy consuming than the rest of the studies in the table.
NiFe LDH intercalated [13h]	ethylene glycol (EG) $Na_2B_4O_7$	NO_3: Cl 4:1	200/12	$\eta_{10}=301$ 42	– 1 M KOH –	
Mo int. NiFe-LDH [13i]	urea (aq.) $(NH_4)_6Mo_7O_{24}$	OAc: NO_3 9:1	160/2-10	$\eta_{10}=280$ 40 mV/dec	Hg/Hg_2Cl_2 1 M KOH, 0.28	
NiFe LDH [11b]	urea (aq.) NF	NO_3 1:1	120/12	$\eta_{30}=280$ 50	– 1 M KOH –	
NiFe LDH [13j]	DMF Carbon quantum dots	OAc: NO_3 1:1	120/12	$\eta_{2.5}=280$ 30	– 1 M KOH –	DMF is not safe for women to use due to infertility links
NiFe HNSs [13k]	water-EG n-butylamine	acac	180/5	$\eta_{10}=220$ 40.7	– 1 M KOH –	n-butylamine is easily flammable and relatively toxic, however the compound reach among the lowest OER potential values in this table
CTAB + Cri-Ni_3Fe [13l]	citric acid-sodium citrate CTAB	Cl 2:1–4:1	140/12	$\eta_{10}=197$ 39	Hg/HgO 1 M KOH –	
Ni_2Fe SDS-LDH/CFP [13m]	ammonium fluoride and urea (aq.) SDS/carbon fiber paper	NO_3 3:1	90/6	$\eta_{10}=285$ 39	Hg/Hg_2Cl_2 1 M KOH 1	
$NiFe_2O_4$ NP/NiFe LDH NSs [13n]	water-methanol sodium carbonate/NF	NO_3: Cl 2:3	120/2	$\eta_{1000}=265$ 28.2	1 M KOH Ag/AgCl 2.8	

sulfate and iron nitrate will be labeled as the "mixed material" sample, Figure 1.

The XRD diffractograms of the three resulting powders are shown in Figure 2. The sulfate, nitrate and mixed material synthesis all show typical peaks of NiFe-LDH (see blue reference pattern). However, according to the salt used, the nature of the secondary phases for each of the NiFe materials changes. The nitrate synthesis contains nickel carbonate ($Ni(CO_3)$)[18] and hematite (Fe_2O_3), Figure 2A. The sulfate synthesis exhibits patterns associated to $Ni(CO_3)$ and α-$Ni(OH)_2$, as well as iron carbonate (siderite, $FeCO_3$), hematite (Fe_2O_3) and goethite (FeOOH), Figure 2B. Furthermore, for this material, there are peaks at 18.30, 30.18, 35.54, 43.45, 57.5 and 63.0° which could either correspond to magnetite Fe_3O_4, nickel ferrite $NiFe_2O_4$ or maghemite γ-Fe_2O_3 which can't be precisely differentiated.[19] The same peaks can be found in the mixed material synthesis which contains the NiFe-LDH as a primary phase and very small peaks corresponding to FeOOH as additional secondary phase, Figure 2C.

The corresponding Raman spectra of the resulting powders are shown in Figure 3. The Raman peaks at 223, 292, 404, 493, 605, 649 and 1313 cm^{-1} visible in both the nitrate and sulfate based synthesis are characteristic vibrational modes of hematite Fe_2O_3.[20] The nitrate material also has a peak at 530 cm^{-1} which can be associated to the NiFe LDH lattice modes and peaks at 1036 and 1114 cm^{-1} characteristic of nickel carbonate anions in the LDH interlayers respectively, which is in good agreement with the XRD in Figure 2.[18,21], The mixed material shows peaks associated to the LDH which are positioned at 294, 458 and 530 cm^{-1} and three typical peaks of $NiFe_2O_4$ at 326, 490 and 695 cm^{-1}.[21a] Therefore, despite the similar XRD pattern in Figure 2 of maghemite Fe_2O_3, magnetite Fe_3O_4 and nickel ferrite $NiFe_2O_4$, the Raman characterization points at the formation of $NiFe_2O_4$ in the case of mixed synthesis.

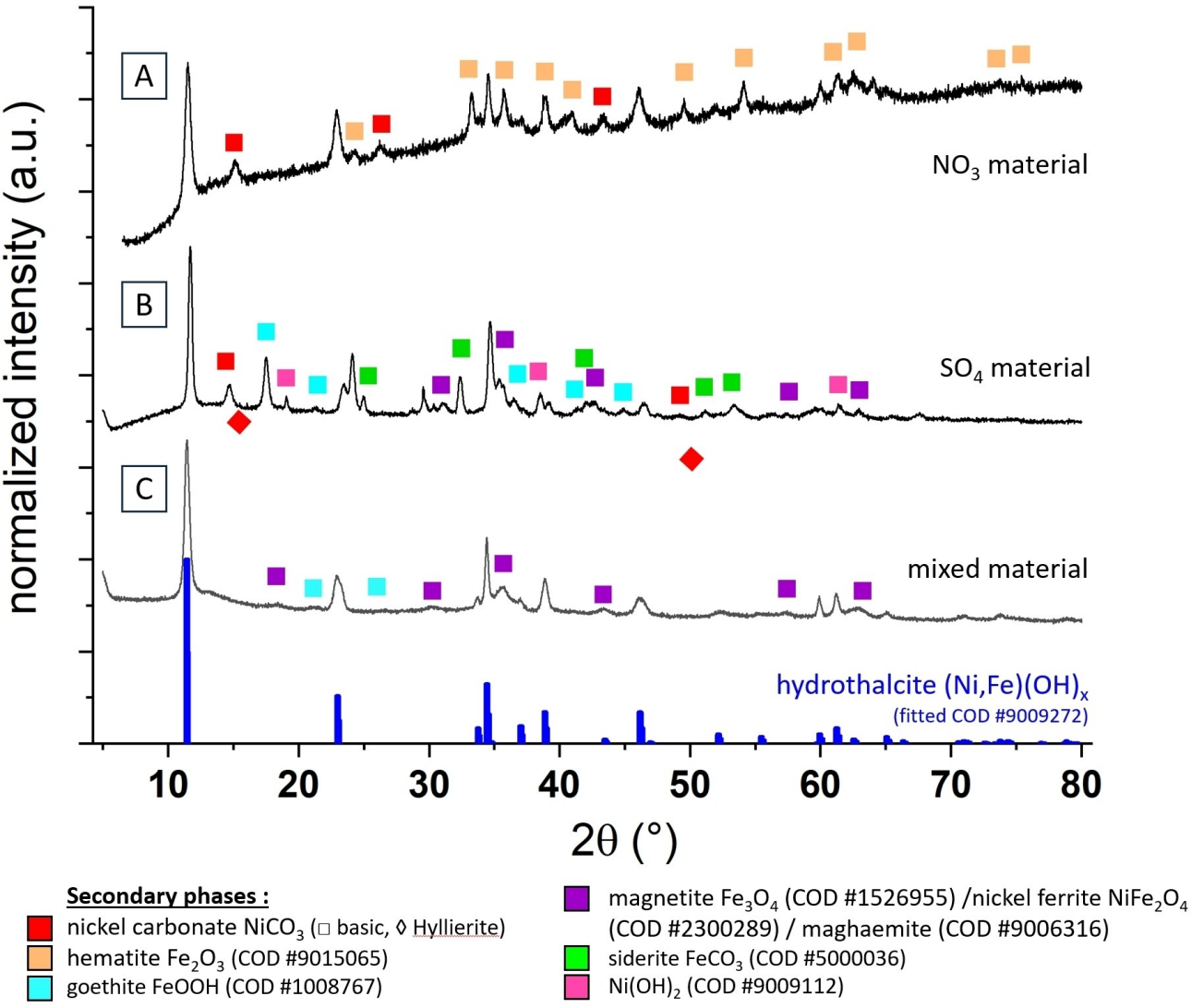

Figure 2. Indexed diffractograms of the resulting A) nitrate, B) sulfate, and C) mixed material synthesis. The XRD pattern in blue is that of hydrotalcite (NiFe LDH). The secondary phases present in the three materials are represented by different colored boxes that can be seen in the XRD diffractogram and the legend underneath.

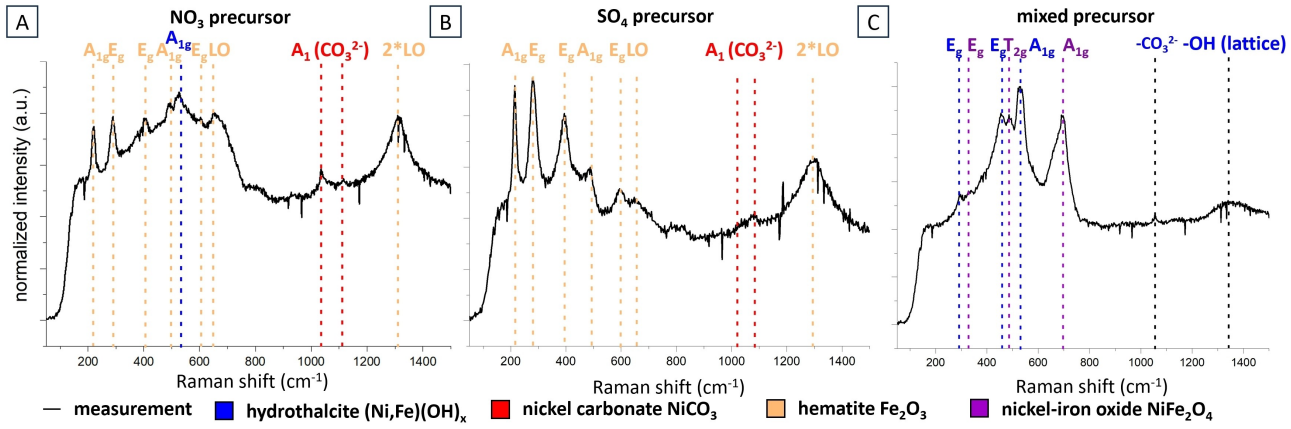

Figure 3. Raman spectra of the resulting A) nitrate, B) sulfate, and C) mixed materials synthesis.

Complementary to the Raman, infrared spectroscopy was also performed and is presented in supplementary material (see S1). The bands at 825, 1063, 1377, 1449 and 1546 cm^{-1} match with carbonate related C–O modes.[18,22] The band at 1635 cm^{-1} are likely due to –OH groups bending modes while the large bands at 3391 and 3450 cm^{-1} are usually assigned to their stretching vibrations modes.[22–23] These bands are in good agreement with the different hydroxide and carbonate species identified by XRD, Figure 2. The M–O modes in FTIR are difficult to assign due to the overlapping nature of these M–O peaks hence Raman spectroscopy is utilized in this study to assigned the M–O peaks.

The precursor influence on the morphology of the materials was investigated by Transmission and Scanning-Transmission Electron Microscopy (TEM/STEM). Representative high-angle annular dark field (HAADF) STEM micrographs of the three powder samples are shown in Figure 4. All samples show large flakes of several hundred nanometers with a space group of $R\bar{3}m$ identified by selected area electron diffraction, matching with the structure of NiFe LDH (see supplementary material S 2). In the case of nitrate material, the flakes have a hexagonal projected shape and are decorated with nanoflowers on the surface, Figure 4A. In comparison, a variety of nanorods, whiskers, columnar grains, and particles aggregated around the flakes were observed in the sulfate synthesis, Figure 4B. These different morphologies could be associated with the different iron carbonates and oxides detected by XRD for the nitrate and sulfate samples in Figure 2. Finally, flakes synthesized from the mixed synthesis, Figure 4C, predominantly had rectangular shapes with nanoflowers covering the surface of the flakes with smaller coverage than the nitrate sample, supposedly associated with the nickel ferrite detected by XRD and Raman.

To access the nature of the structures observed from the STEM observations, detailed EDS mapping and analysis of the different morphologies were carried out, shown in Figure 5. The STEM-EDS map of the nanoflower-like particles on the flakes of the nitrate-based synthesis (Figure 5A) allows to differentiate both monometallic species detected in XRD. One can easily differentiate isolated iron (blue) and nickel (yellow) particles (circled) as a proof for the presence of $Ni(CO_3)$ and Fe_2O_3 on the NiFe LDH. The elemental maps of whiskers in the sulfate material (Figure 5B) shows that the flakes are not the only bimetallic species in the sample. The carbon signal found in the whiskers, as well as the trigonal space group determined by

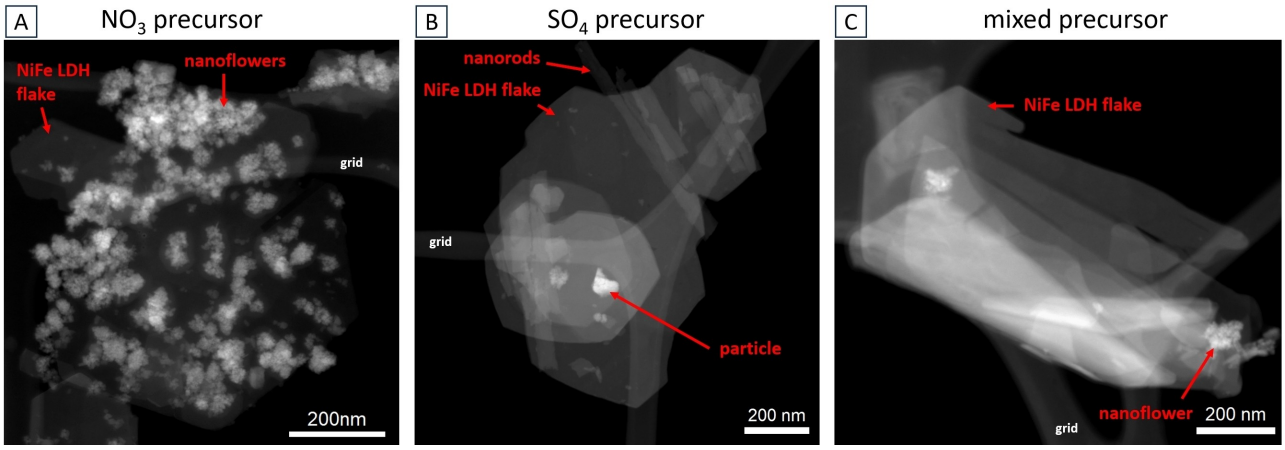

Figure 4. Representative HAADF-STEM micrographs of the particles in the A) nitrate, B) sulfate and C) mixed material synthesis.

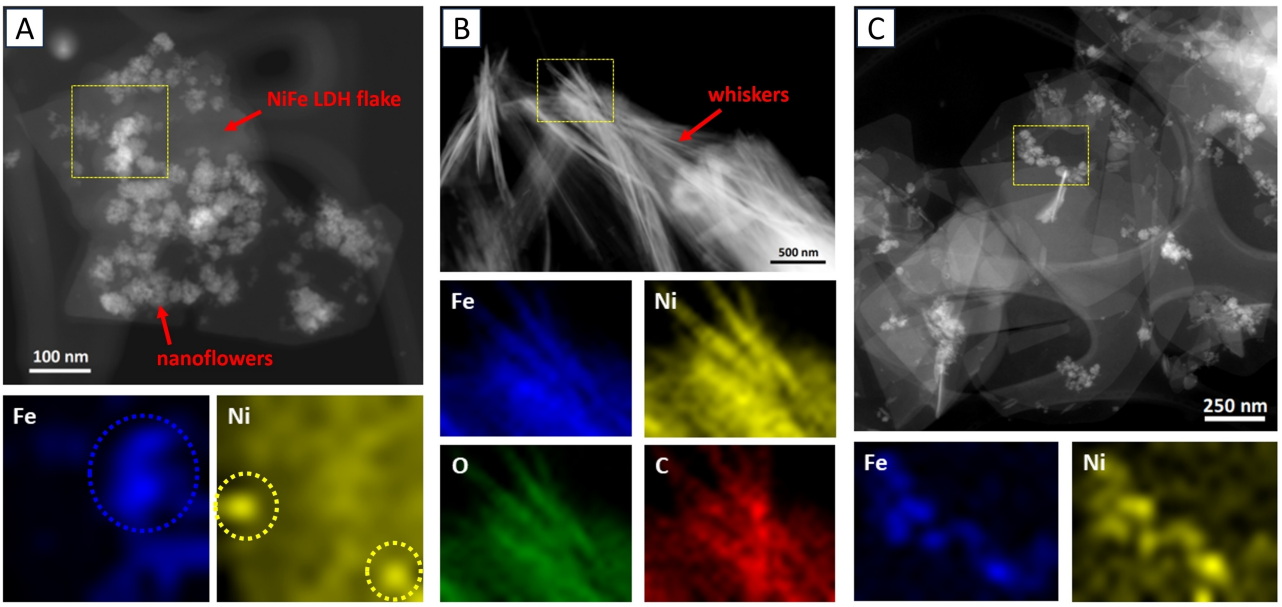

Figure 5. Z-contrast STEM images and corresponding EDS maps Z-contrast STEM images and corresponding EDS maps of the particles in the A) nitrate, B) sulfate and C) mixed material synthesis.

SAED, could mean that the nickel was able to incorporate in the structure of the iron carbonates/oxides. The EDS mapping of the nanoflowers in the mixed material sample confirms the bimetallic nature of the compound which confirms the presence of $NiFe_2O_4$, Figure 5C.

The high-resolution X-Ray photoelectron Spectroscopy (XPS) Ni $2p_{3/2}$ and O 1 s regions of the nitrate, sulfate and mixed materials are shown in Figure 6. From the Ni 2p region, Figure 6A, the measured spectrum is similar to that of a Ni material that exhibits an oxidation state of 2+. As $NiFe_2O_4$, $Ni(OH)_2$ and NiFe LDH all exhibit Ni^{2+} species it would be difficult to pinpoint what of these materials are present and in what amounts.[8e,24]

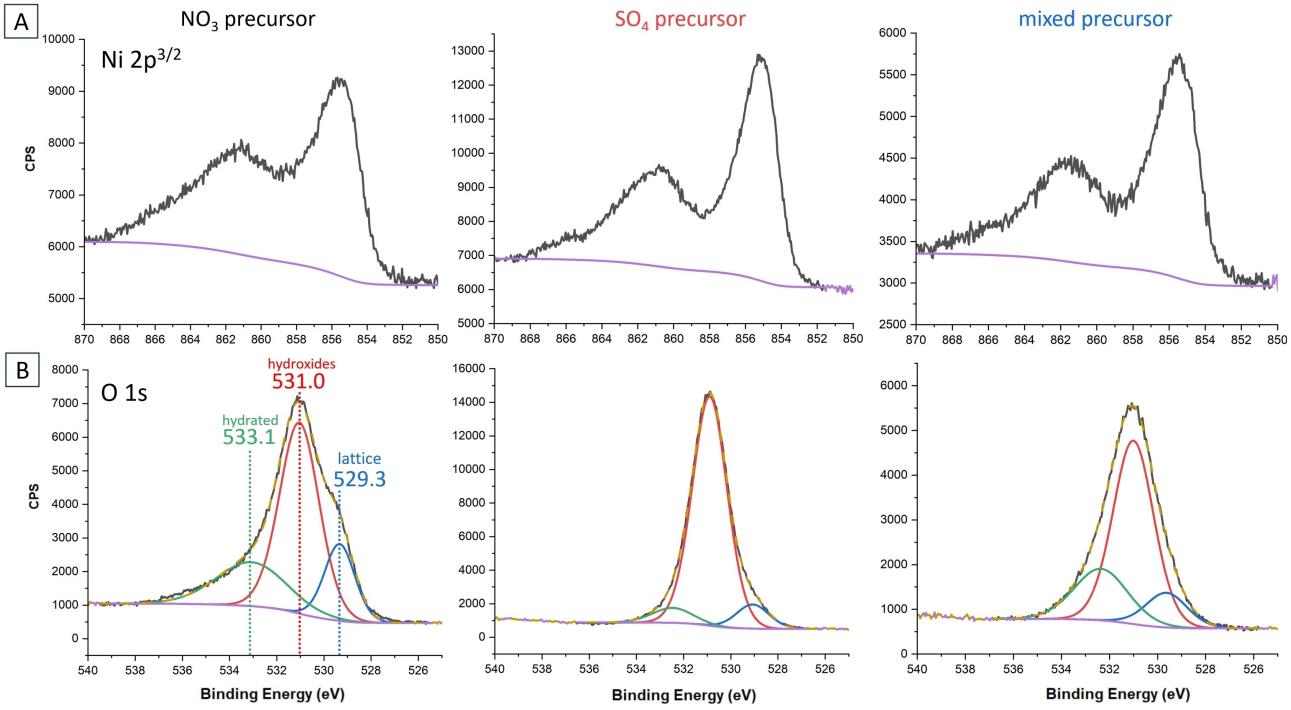

Figure 6. XPS spectra of the A) Ni $2p^{3/2}$ and B) O 1 s regions for the nitrate, sulfate, and mixed materials.

However, more information can be elucidated from the O 1 s region about the presence of various oxides in each of the materials, Figure 6B. The sulfate and mixed materials exhibit similar O 1 s regions however there is a large contribution of the hydroxide O 1 s peak (~531 eV) for the sulfate materials which could explain the present of the $Ni(OH)_2$ from the XRD, Figure 2B.[25] For the nitrate O 1 s region, the significant increase in the lattice and hydrated O 1 s compared to the sulfate and mixed materials may be due to the presence of the large quantity of Fe_2O_3 in this material which exhibits a lattice and hydrated O 1 s peak at 529.9 and 532.5 eV, respectively.[25] This is also consistent with the XRD data for the nitrate materials in Figure 2.

From the materials characterization, Figure 2–6, it can be determined that the metal salt material has a significant effect on the material's final transformation. To further discuss the influence of the precursor, the corresponding monometallic sulfate and nitrate materials were synthesized and characterized, showing that each precursor results in a different phase. From XRD and Raman spectroscopy (see supplementary material S3),, the synthesis with the Fe and Ni nitrate salt only leads to the formation of hematite and nickel basic carbonate, respectively. Interestingly, using Fe or Ni sulfate salt only results in a mix of iron species (hematite, siderite, magnetite, goethite) and nickel hydroxide, respectively.

Now utilizing this information and relating it to the secondary phases in the bimetallic nitrate and sulfate materials obtained, one can directly see the close relationship with the corresponding monometallic synthesis. The nitrate synthesis' secondary phases consist in hematite and nickel basic carbonate, while the sulfate synthesis contains a mix of monometallic oxides, hydroxides, and carbonate similarly to the monometallic iron sulfate synthesis. As for the mixed synthesis, the few secondary phases correspond to iron hydroxide and nickel ferrite, the latest formation being maybe promoted by the mix of anion. For comparison purpose, a "twin" synthesis of the mixed material was made inverting the nitrate and sulfate source; the only difference is the formation of iron carbonate, pointing at the iron sulfate as a carbonate formation driving factor (see supplementary S4). The results of the different phases formed by varying the metal salts in the same hydrothermal synthesis are summarized in Table 2.

Electrochemical Characterization

To assess how the various NiFe materials made by using various metal salts effects the OER, a suite of electrochemical tests was performed in 1 M NaOH. In Figure 7 the cyclic voltammograms of the three materials are presented. Both the nitrate and sulfate materials show an oxidation peak around 0.45 V vs. Hg/HgO which can be attributed to a Ni^{2+}/Ni^{3+} transitions.[26] This peak is usually shifted to more anodic potentials and almost incorporated into the OER region for mixed NiFe materials as in Figure 7C for the mixed material.[8b] This result would indicate that the nitrate and sulfate only NiFe based materials also contain a significant amount of Ni based materials compared to the mixed NiFe based material.

Table 2. Occurrence of each phase according to the precursor.

Phase | precursor	$Fe(SO_4)$	$Fe(NO_3)_3$	$Ni(SO_4)$	$Ni(NO_3)_2$	$Ni(NO_3)_2$ $Fe(NO_3)_3$	$Ni(SO_4)$ $Fe(SO_4)$	$Ni(SO_4)$ $Fe(NO_3)_3$	$Ni(NO_3)_2$ $Fe(SO_4)$
α-Fe_2O_3	●	●			●			
$NiFe_2O_4/Fe_3O_4$	●					●	●	●
FeOOH	●					●	●	●
$FeCO_3$	●					●		●
$NiCO_3$				●	●	●		
$Ni(OH)_2$			●					
NiFe LDH					●	●	●	●

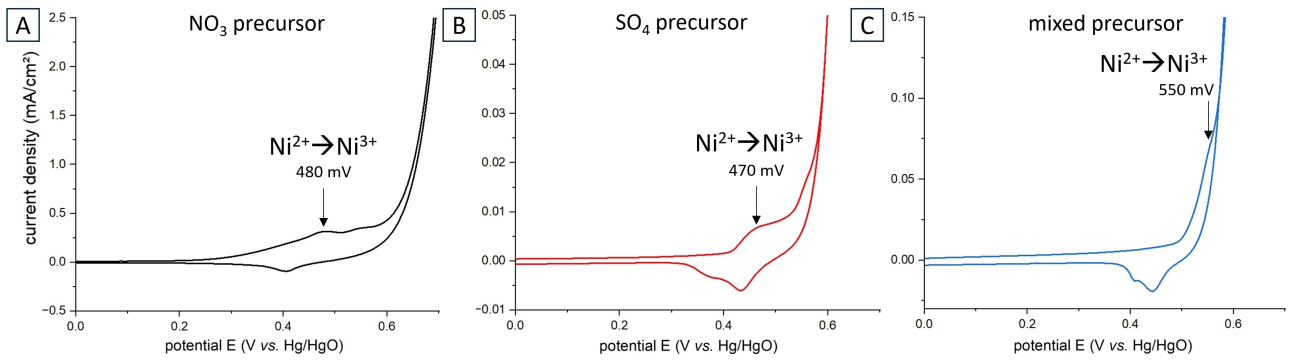

Figure 7. Cyclic Voltammetry of the A) nitrate B) sulfate and C) mixed material synthesis (5th cycle). The NaOH electrolyte only contains Na_2CO_3 as an impurity.

The OER activity at a current density of 10 mA cm^{-2} was determined from Linear Sweep Voltammetry (LSV) measurements in Figure 8A. It is evident that the nickel-iron bimetallic materials performance depends on the nature of the precursor salt. The two single-salt synthesis (sulfate-only and nitrate-only) exhibit overpotential values of 460 and 425 mV, respectively, at a current density of 10 mA cm^{-2} while the mixed materials performance is better and exhibits an overpotential of 346 mV at the same current density, see Figure S5 for reproducibility LSV curves for all materials.

The decrease in the OER performance of the NiFe material synthesized by the sulfate-only and nitrate-only precursors may be due to the present of the single phase Fe_2O_3 and the pure Ni^{2+} materials, $Ni(CO_3)$ and $Ni(OH)_2$, from Table 2. This is hypothesized by the redox peaks in the CV curves as the Ni^{2+}/$^{3+}$transition for the sulfate-only and nitrate-only is at lower potentials compared with the mixed materials and results in

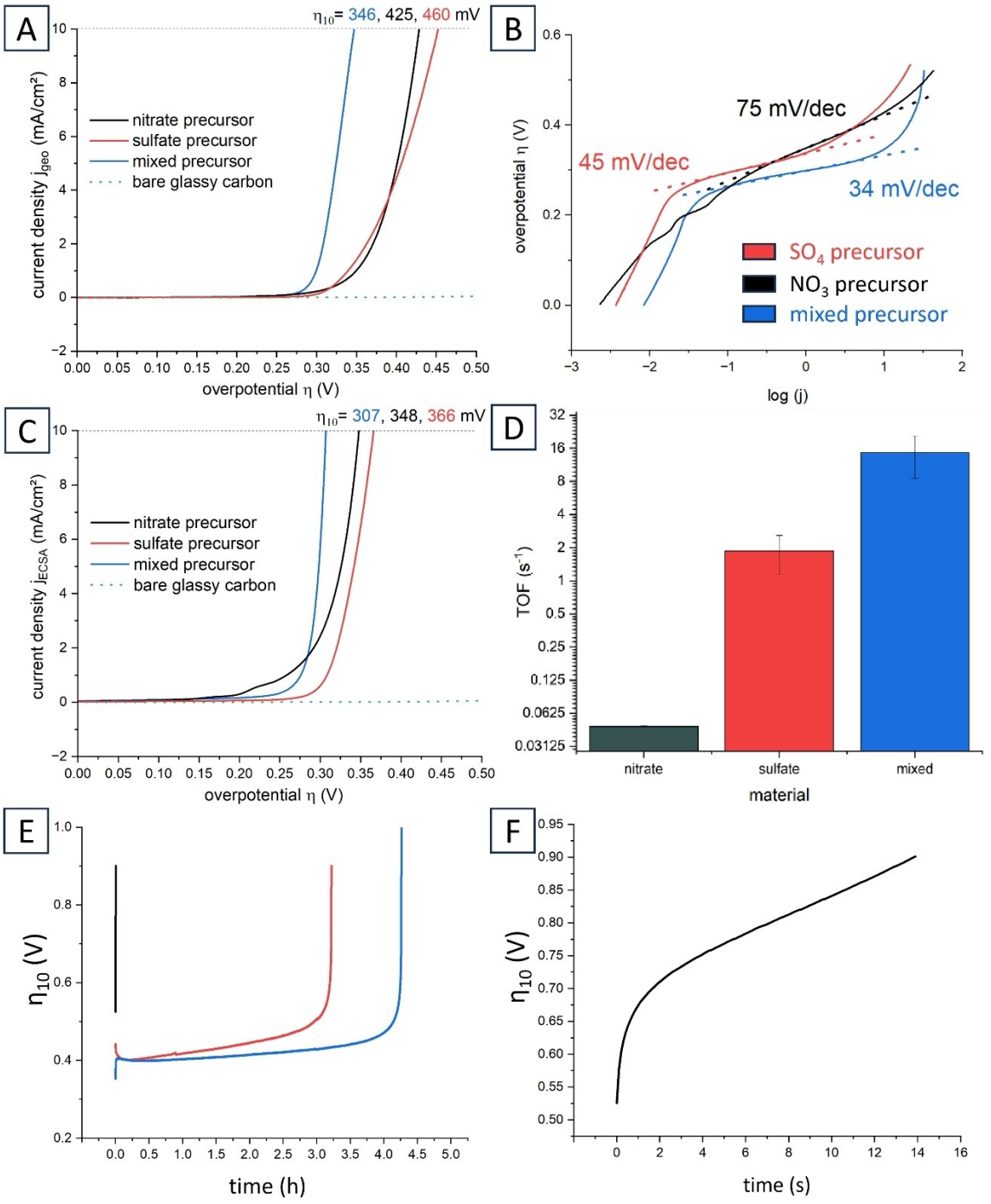

Figure 8. A) Linear Sweep Voltammetry, B) Tafel slope, C) electrochemical surface area-normalized LSV, D) TOF, E) stability test of the nitrate, sulfate, and mixed material synthesis with F) a zoom for the nitrate-based synthesis (black curve). The reproduction of the measures for the Linear Sweep Voltammetry and ECSA measurements are shown in supplementary material S5 and S6.

lower OER performances. Furthermore, the mixed materials also yield the best Tafel slope in this study, Figure 8B, again showing improved OER performance compared to the sulfate-only and nitrate-only NiFe materials. The Tafel slopes for the mixed, sulfate and nitrate materials are 34, 45 and 75 mV/dec, respectively. These values are comparable to the one reported for NiFe LDH materials (see Table 1), ranging from 21 to 59 mV/dec, which suggest that the OER activity of the electrode is mainly driven by the NiFe LDH. These unusually low Tafel slope values (30 mV/dec) for NiFe LDH have already been associated with the dehydrogenation of the metal peroxide being the rate determining step of the reaction ($MOOH + OH^- \rightarrow MOO^- + H_2O$).[27] The higher value in the case of the nitrate and sulfate materials can be explained by the higher amount of iron based secondary phases, which typically display Tafel slopes ranging from 40 to 60 mV/dec according to their hydration states.[28]

The electrochemical surface area-normalized current on Figure 8C shows an improved overpotential at a current density of 10 mA cm^{-2} for all samples but the trend is the same as in the geometric area normalized LSV curves. The optimum catalyst remains the mixed material but the nitrate and sulfate material both show a 100 mV overpotential difference compared to the geometric area normalized current. The mixed material also displays an impressive Turnover Frequency (TOF) compared to the sulfate only and nitrate only materials, figure 8D. The TOF for the mixed, sulfate and nitrate materials at an overpotential of 0.32 V are 14.6, 1.9, and 0.05 s^{-1} respectively.

The stability tests in Figure 8E demonstrates how the choice of precursors effects the OER over time at a fixed current density (10 mA cm^{-2}) and hence highlights the critical choice of the precursor. The nitrate-based synthesis degrades at a tremendous rate with a rapid OER overpotential decrease once the current density is applied.[4] The sulfate material shows an increased stability compared to the nitrate materials however becomes deactivated at about 3.5 hours of applied current density. The mixed material is the optimum catalyst in terms of stability, however, it degrades overtime which is consistent with literature reports.[9b] Nevertheless, these tests illustrate the intrinsic instability of these materials but also how the choice of precursor is a factor in the lifetime of a material.[9] This stability and the overall better behaviour of the mixed oxide synthesis is more than likely due to the presence of the LDH and the minimum presence of secondary phases.

In order to gain insight into the rapid decline of the stability for the NiFe nitrate material, post-mortem microstructural analysis was carried out on spraycoated electrodes of the materials after exposition to OER conditions (see S7–S9). The SEM images of the three materials showed no noticeable morphological change of the particles before and after OER. The XPS spectra of the spraycoated samples almost superpose, confirming an overall consistency of the surface chemistry of the materials. Similarly, the Raman peaks of the different phases remain the same, meaning that metal-oxygen bonds are not changed. Interestingly, the diffractograms also shows that the phases of the sulfate and mixed material are unchanged, however the disappearance of a strong diffraction peak associated to hematite in the case of the nitrate synthesis confirms that the hematite is dissolving (see yellow circle in Figure 9). Hematite is prone to dissolve in concentrated base and even more in NaOH compared to other alkaline media,[29] which can lead to breaking of the catalytic film, as the hematite grows directly on the LDH flakes (see figure 5).

Considering the entirety of the electrochemical characterization, one can conclude that the presence of iron oxide secondary phase in in the samples seems to be a limiting factor for the electron transfer step as well as the general activity of the catalyst. Indeed, the pure Fe_2O_3 present in the nitrate-based synthesis could be associated with the poor performance of the corresponding catalyst, potentially hindering the hydrothalcite structure sheets electron transfer. The TEM observation makes it clear that the hematite grows on the LDH, covering it as a flourishing field of deadly flowers. In a similar way, the nanorods and other particles observed in the sulfate-based synthesis of NiFe LDH seem to have a detrimental effect on its activity. However, there is consistency between the effect of the iron species (sulfate vs nitrate-based synthesis), as the mix of siderite/goethite/magnetite allows a better reaction rate than the hematite, which is in good agreement with the general trends in the activity of iron oxides.[30]

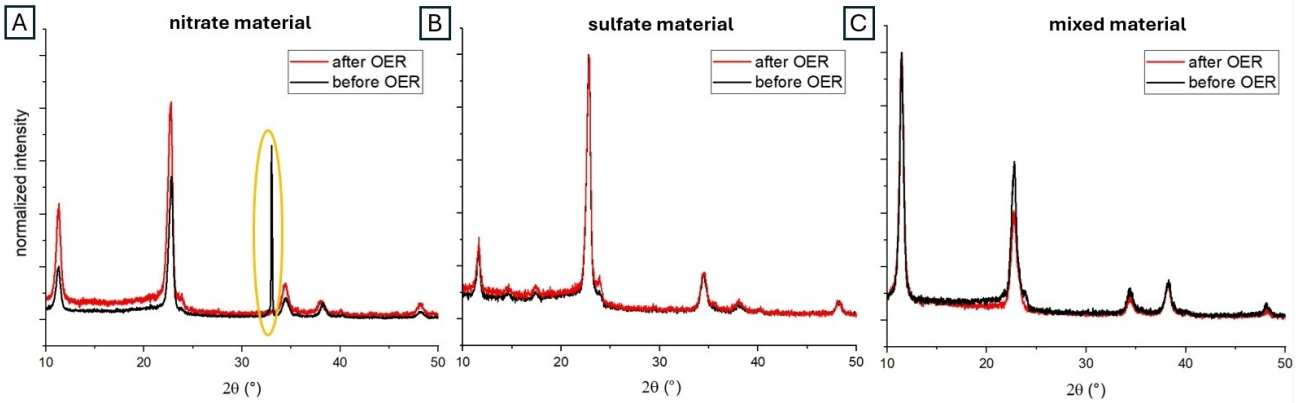

Figure 9. Diffractograms of the A) nitrate, B) sulfate, and C) mixed materials before and after OER conditions.

Conclusions

In this study, we use a facile route for the synthesis of NiFe pre-catalyst mix without using organic solvent, additive or support to study the effects of the metal salt precursors. This simple urea synthesis route demonstrated how different materials products can be synthesized due to the nature of the precursors used. The presence or growth of secondary phases in the catalysts, in particular Fe_2O_3 and single-phase nickel-based materials, seem to be the hindering source for the decrease activity of NiFe LDH. These results allow for a better understanding of the influence of the precursor on the product, which proportions could then be optimized to target purer material. Interestingly, while the three syntheses had the same amount of urea and precursor salts, only the mixed material synthesis displayed a low amount of mixed iron and nickel secondary phases which is clearly needed not to hinder the OER.

Methods

Hydrothermal Synthesis

The hydrothermal syntheses were performed in a facile route using nitrate and/or sulfate metal salts ($Fe(NO_3)_3 \cdot 9H_2O$, $FeSO_4 \cdot 7H_2O$, $Ni(NO_3)_2 \cdot 6H_2O$, $NiSO_4 \cdot 6H_2O$, $>99.5\,\%$, SigmaAldrich), urea and water with a salt : urea = 1 : 5 ratio at a 0.66 mol/L concentration of urea. Practically, it traduces in 0.004 mol of salt and 0.02 mol of urea dissolved in 30 mL of water for a synthesis in a 45 mL Teflon liner. The stainless-steel autoclave is then sealed and put in a cold oven. The oven is then heated at 120 °C for 18 hours after which the heating stops, and the system is let to cool down naturally. The resulting powder is then washed with DI water in a centrifuge until the pH reaches neutral and let to dry overnight in an oven at 60 °C.

Microstructure Characterization

The samples were characterized using a D8 X-Ray diffractometer (Bruker) with a copper source. The data presented in the manuscript are raw, meaning a slight broadening/shouldering can result from the presence of the two K-α radiations of the copper. The particles morphologies of the samples were observed using a Karl Zeiss MERLIN scanning electron microscope (SEM) equipped with a field emission gun. The Raman spectra were measured using an i-Raman Plus 532H portable Raman spectrometer (532 nm, 100 % intensity). The FT-IR spectra were acquired using a BRUKER ALPHA compact FT-IR spectrometer. Transmission electron microscopy (TEM) observations were performed on JEOL 2100 LaB_6 operated at 200 kV. Scanning-TEM (STEM) observations were performed on FEI Titan 80–300 kV FEG S/TEM and EDX data were acquired in digital micrograph (GMS2) using a Bruker XFlash 6T-30 detector. The powder samples were dispersed in isopropanol and put in ultrasonication for 15 minutes. Three drops were drop-casted in a TED PELLA lacey Carbon grid and left to dry in room temperature. XPS measurements were obtained using an Omicron EA 125 Energy Analyzer with a monochromated Al K-alpha source at 1486.7 eV. High resolution core level component XPS scans were obtained with a pass energy of 20 eV, high magnification mode, entrance and exit slits of 6 mm and 3 mm, respectively, giving an overall source and instrument resolution of 0.6 eV. Low resolution (survey scans) measurements were obtained with a pass energy of 50 eV, high magnification mode, entrance and exit slits of 6 mm and 6 mm, respectively, giving an overall source and instrument resolution of 1.5 eV.

Electrochemical Characterization

Electrochemical tests were performed with a VIONIC Autolab potentiostat (Metrohm) connected to a RRDE 3 A setup (ALS-Japan). The powder material obtained by hydrothermal synthesis was dispersed into an ink of a water : ethanol = 1 : 1 mix containing 8 μL/mL of Nafion. The ink was drop casted on 3 mm diameter glassy carbon electrodes (ALS-Japan) to get a mass loading of 1.6 mg/cm^2. The measurements were conducted in a 1 M NaOH electrolyte (NaOH ≥ 98 % anhydrous pellets, Sigma Aldrich, Impurities: $Na_2CO_3 \leq 1\,\%$) and with a carbon rod as counter electrode. Cyclic Voltammetry was conducted for 5 cycles between −0.2 and 0.6 V vs. Hg/HgO. Electrochemical impedance spectroscopy was performed in a non-Faradaic region from 5 Hz to 100 kHz. Electrochemical surface area measurements were conducted using cyclic voltammetry in a 0.1 V non-faradaic region at 100, 50, 20, 10, 5 mV/s (see supplementary S5 for the results). Linear sweep voltammetry was carried out from 0 to 0.85 V *vs.* Hg/HgO at a scan rate of 1 mV/s.

All measurements were performed against Hg/HgO reference electrode. The value of the real part of the impedance measurements at 100 kHz was used to define the solution resistance (R_u), which was used to correct the potential of the linear sweep voltammetry curves showed in this paper ($E_{corr} = E\text{-}iR_u$). The current density j_{geo} was calculated by dividing the current (I) by the geometrical area of the electrode (~0.07 cm^2) and the Tafel slopes were calculated by linear regression of the $\eta = f(\log(j))$ curve in the 10 mA/cm^2 benchmark region ($\eta = E + E_{Hg/HgO}(pH = 14) - 1.23$). The capacitance of the film was determined from the slope of the current vs. scan rate curve at a given potential. The capacitance allows to estimate the electrochemical surface area (A_{ECSA}) by dividing it by the specific capacitance of TMOs (0.00004 F). The roughness factor was calculated such as: $RF = A_{ECSA}/A_{geo}$. The TOF of the nickel and nickel-iron catalysts was further calculated by taking LSV current at 0.35 V divided by the charge value. The charge was deduced from the integrated area of the last cycle of the catalyst preconditioning (from 0 V *vs.* Hg/HgO to a potential before the OER region) divided by the scan rate. The stability tests were carried out at 10 mA cm^{-2} until degradation of the material.

Post-Mortem Analysis

Post-mortem analysis of the samples was carried out by preparation of spray-coated electrodes with the different materials. The ink prepared as indicated in the electrochemical characterization part was spray-coated on a titanium coated silicon wafer and let to dry. These electrodes were characterized before and after undergoing the electrochemical characterization described above. The XRD and SEM images were acquired as mentioned above. The Raman spectra were acquired using a i-Raman Plus 785S portable Raman spectrometer (785 nm, 40 % intensity). The X-ray photoelectron spectroscopy (XPS) measurements were conducted using a JEOL JPS-9030 setup. A non-monochromated Al source with 300 W power was used for excitation and a hemispherical analyzer with pass energy of 50 eV (surveys) and 20 eV (narrow scans) was used to detect the emitted photoelectrons.

Supporting Information

A supporting information document is available for this work in a separate file.

Acknowledgements

We gratefully acknowledge the Helmholtz Association's Initiative and Networking Fund (Helmholtz Young Investigator Group VH-NG-1719) for the funding. VN wishes to acknowledge funding from the European Research Council (CoG 3D2Dprint, GA681544), Science Foundation Ireland (12/RC/2278_P2 and 16/RC/3872_P2, Frontiers for the Future 20/FFP–A/8950), and HORIZON-RIA 101091572 GREENCAP. P.W.M and M.P.B greatly acknowledge support from the German Federal Ministry of Education and Research in the framework of the project Catlab (03EW0015 A/B). LG and IC acknowledge support from the Irish Research Council (grant GOIPG/2020/1250) and the Provosts PhD Research Project respectively for funding. VN and IMO acknowledge support from the European Union's Horizon 2020 research and innovation program under Agreement No. 956813.

The authors would like to address particular thanks to R. Schwiddessen, M. Tovar, K. Schwartzburg and M. Wollgotten from the X-Ray and Microscopy and Spectroscopy corelabs of the Helmholtz Zentrum Berlin for providing access to their facility and training on the equipment. The authors would like to acknowledge CRANN and AMBER research centers, as long Advanced Microscopy Laboratory (AML) for access to their infrastructure. Open Access funding enabled and organized by Projekt DEAL. Open Access funding provided by IReL.

Conflict of Interests

The authors declare no conflict of interest.

Data Availability Statement

The data that support the findings of this study are available from the corresponding author upon reasonable request.

Keywords: water splitting · oxygen evolution reaction · hydrothermal synthesis · precursors · NiFe LDH

[1] *IPCC*, (Ed.: H. L. a. J. Romero), IPCC, **2023**.
[2] *IEA*, IEA, Paris **2022**.
[3] a) I. Roger, M. A. Shipman, M. D. Symes, *Nat. Chem. Rev.* **2017**, *1*, 0003; b) Y. Yan, B. Y. Xia, B. Zhao, X. Wang, *J. Mater. Chem. A* **2016**, *4*, 17587–17603; c) M. Chatenet, B. G. Pollet, D. R. Dekel, F. Dionigi, J. Deseure, P. Millet, R. D. Braatz, M. Z. Bazant, M. Eikerling, I. Staffell, P. Balcombe, Y. Shao-Horn, H. Schäfer, *Chem. Soc. Rev.* **2022**, *51*, 4583–4762.
[4] a) L. Zhang, Q. Fan, K. Li, S. Zhang, X. Ma, *Sustain. Energy Fuels* **2020**, *4*, 5417–5432; b) M. E. G. Lyons, M. P. Brandon, *J. Electroanal. Chem.* **2010**, *641*, 119–130; c) R. Subbaraman, D. Tripkovic, K.-C. Chang, D. Strmcnik, A. P. Paulikas, P. Hirunsit, M. Chan, J. Greeley, V. Stamenkovic, N. M. Markovic, *Nat. Mater.* **2012**, *11*, 550–557; d) I. C. Man, H.-Y. Su, F. Calle-Vallejo, H. A. Hansen, J. I. Martínez, N. G. Inoglu, J. Kitchin, T. F. Jaramillo, J. K. Nørskov, J. Rossmeisl, *ChemCatChem* **2011**, *3*, 1159–1165; e) M. S. Burke, S. Zou, L. J. Enman, J. E. Kellon, C. A. Gabor, E. Pledger, S. W. Boettcher, *J. Phys. Chem. Lett.* **2015**, *6*, 3737–3742; f) M. Schalenbach, A. R. Zeradjanin, O. Kasian, S. Cherevko, K. J. J. Mayrhofer, *Int. J. Electrochem. Sci.* **2018**, *13*, 1173–1226.
[5] a) M. Görlin, P. Chernev, J. Ferreira de Araújo, T. Reier, S. Dresp, B. Paul, R. Krähnert, H. Dau, P. Strasser, *J. Am. Chem. Soc.* **2016**, *138*, 5603–5614; b) S. Chen, L. Ma, Z. Huang, G. Liang, C. Zhi, *Cell Reports Physical Science* **2022**, *3*, 100729; c) S. Anantharaj, K. Karthick, S. Kundu, *Mater. Today* **2017**, *6*, 1–26; d) A. Moysiadou, S. Lee, C.-S. Hsu, H. M. Chen, X. Hu, *J. Am. Chem. Soc.* **2020**, *142*, 11901–11914.
[6] a) P. Connor, J. Schuch, B. Kaiser, W. Jaegermann, *ZPC* **2020**, *234*, 979–994; b) M. P. Browne, Z. Sofer, M. Pumera, *Energy Environ. Sci.* **2019**, *12*, 41–58.
[7] a) D. A. Corrigan, *J. Electrochem. Soc.* **1987**, *134*, 377; b) W. J. Hunter, *Molecules* **2018**, *23*.
[8] a) F. Dionigi, P. Strasser, *Adv. Energy Mater.* **2016**, *6*, 1600621; b) L. Trotochaud, S. L. Young, J. K. Ranney, S. W. Boettcher, *J. Am. Chem. Soc.* **2014**, *136*, 6744–6753; c) F. Dionigi, Z. Zeng, I. Sinev, T. Merzdorf, S. Deshpande, M. B. Lopez, S. Kunze, I. Zegkinoglou, H. Sarodnik, D. Fan, A. Bergmann, J. Drnec, J. F. d. Araujo, M. Gliech, D. Teschner, J. Zhu, W.-X. Li, J. Greeley, B. R. Cuenya, P. Strasser, *Nat. Commun.* **2020**, *11*, 2522; d) Y. Liu, X. Lei, B. Xiong, J. Chen, W. Zou, Z. Fu, Y. Lu, *J. Chem. Res.* **2022**, *46*, 17475198221103519; e) D. Tyndall, S. Jaskaniec, B. Shortall, A. Roy, L. Gannon, K. O'Neill, M. P. Browne, J. Coelho, C. McGuinness, G. S. Duesberg, V. Nicolosi, *NPJ 2D Mater. Appl.* **2021**, *5*, 73; f) H. Yi, S. Liu, C. Lai, G. Zeng, M. Li, X. Liu, B. Li, X. Huo, L. Qin, L. Li, M. Zhang, Y. Fu, Z. An, L. Chen, *Adv. Energy Mater.* **2021**, *11*, 2002863; g) M. Gong, H. Dai, *Nano Res.* **2015**, *8*, 23–39; h) R. Gao, D. Yan, *Adv. Energy Mater.* **2020**, *10*, 1900954; i) L. Trotochaud, J. K. Ranney, K. N. Williams, S. W. Boettcher, *J. Am. Chem. Soc.* **2012**, *134*, 17253–17261.
[9] a) T. Binninger, R. Mohamed, K. Waltar, E. Fabbri, P. Levecque, R. Kötz, T. J. Schmidt, *Sci. Rep.* **2015**, *5*, 12167; b) D. Tyndall, M. J. Craig, L. Gannon, C. McGuinness, N. McEvoy, A. Roy, M. García-Melchor, M. P. Browne, V. Nicolosi, *J. Mater. Chem. A* **2023**, *11*, 4067–4077.
[10] a) G. Y. Abo El-Reesh, A. A. Farghali, M. Taha, R. K. Mahmoud, *Sci. Rep.* **2020**, *10*, 587; b) J. Qiao, F. Song, J. Hu, D. Huo, J. Yuan, J. Shen, L. Niu, A.-j. Wang, *Int. J. Hydrogen Energy* **2019**, *44*, 16368–16377; c) S. Jaśkaniec, C. Hobbs, A. Seral-Ascaso, J. Coelho, M. P. Browne, D. Tyndall, T. Sasaki, V. Nicolosi, *Sci. Rep.* **2018**, *8*, 4179; d) C. Hou, Z. Cui, S. Zhang, W. Yang, H. Gao, X. Luo, *RSC Adv.* **2021**, *11*, 37624–37630; e) J. Qi, W. Zhang, R. Xiang, K. Liu, H.-Y. Wang, M. Chen, Y. Han, R. Cao, *Adv. Sci.* **2015**, *2*, 1500199; f) J. L. Gunjakar, A. M. More, K. V. Gurav, C. D. Lokhande, *Appl. Surf. Sci.* **2008**, *254*, 5844–5848.
[11] a) F. J. Pérez-Alonso, C. Adán, S. Rojas, M. A. Peña, J. L. G. Fierro, *Int. J. Hydrogen Energy* **2014**, *39*, 5204–5212; b) Z. Lu, W. Xu, W. Zhu, Q. Yang, X. Lei, J. Liu, Y. Li, X. Sun, X. Duan, *Chem. Commun.* **2014**, *50*, 6479–6482; c) M. D. Merrill, R. C. Dougherty, *J. Phys. Chem. C* **2008**, *112*, 3655–3666; d) K. H. Kim, J. Y. Zheng, W. Shin, Y. S. Kang, *RSC Adv.* **2012**, *2*, 4759–4767; e) S. H. Ahn, I. Choi, H.-Y. Park, S. J. Hwang, S. J. Yoo, E. Cho, H.-J. Kim, D. Henkensmeier, S. W. Nam, S.-K. Kim, J. H. Jang, *Chem. Commun.* **2013**, *49*, 9323–9325; f) S. Zhuang, L. Wang, H. Hu, Y. Tang, Y. Chen, Y. Sun, H. Mo, X. Yang, P. Wan, Z. U. H. Khan, *ChemElectroChem* **2018**, *5*, 2577–2583.
[12] a) L. Yu, J. F. Yang, B. Y. Guan, Y. Lu, X. W. Lou, *Angew. Chem. Int. Ed.* **2018**, *57*, 172–176; b) R. Wang, C. Wang, S. Yin, Y. Peng, J. Chen, Y. Deng, J. Li, *Catal. Today* **2021**, *364*, 140–147.
[13] a) S. P. Keerthana, R. Yuvakkumar, G. Ravi, T. S. Senthil, M. Pannipara, A. G. Al-Sehemi, D. Velauthapillai, *Applied Nanoscience* **2021**, *11*, 2669–2677; b) R. Li, J. Xu, Q. Pan, J. Ba, T. Tang, W. Luo, *ChemistryOpen* **2019**, *8*, 1027–1032; c) Z. Zhang, C. Wang, X. Ma, F. Liu, H. Xiao, J. Zhang, Z. Lin, Z. Hao, *Small* **2021**, *17*, 2103785; d) K. Fominykh, P. Chernev, I. Zaharieva, J. Sicklinger, G. Stefanic, M. Döblinger, A. Müller, A. Pokharel, S. Böcklein, C. Scheu, T. Bein, D. Fattakhova-Rohlfing, *ACS Nano* **2015**, *9*, 5180–5188; e) F. Dionigi, T. Reier, Z. Pawolek, M. Gliech, P. Strasser, *ChemSusChem* **2016**, *9*, 962–972; f) M. Gong, Y. Li, H. Wang, Y. Liang, J. Z. Wu, J. Zhou, J. Wang, T. Regier, F. Wei, H. Dai, *J. Am. Chem. Soc.* **2013**, *135*, 8452–8455; g) F. Song, X. Hu, *Nat. Commun.* **2014**, *5*, 4477; h) L. Su, H. Du, C. Tang, K. Nan, J. Wu, C. Ming Li, *J. Colloid Interface Sci.* **2018**, *528*, 36–44; i) N. Han, F. Zhao, Y. Li, *J. Mater. Chem. A* **2015**, *3*, 16348–16353; j) D. Tang, J. Liu, X. Wu, R. Liu, X. Han, Y. Han, H. Huang, Y. Liu, Z. Kang, *ACS Appl. Mater. Interfaces* **2014**, *6*, 7918–7925; k) X. Sun, Q. Shao, Y. Pi, J. Guo, X. Huang, *J. Mater. Chem. A* **2017**, *5*, 7769–7775; l) Y. Li, Y. Gao, M. Liu, T. Wang, X. Wang, H. Hu, *Int. J. Electrochem. Sci.* **2022**,

17, 220338; m) H. Zhong, X. Cheng, H. Xu, L. Li, D. Li, P. Tang, N. Alonso-Vante, Y. Feng, *Electrochim. Acta* **2017**, *258*, 554–560; n) Z. Wu, Z. Zou, J. Huang, F. Gao, *ACS Appl. Mater. Interfaces* **2018**, *10*, 26283–26292.
[14] W. Zheng, M. Liu, L. Y. S. Lee, *ACS Energy Lett.* **2020**, *5*, 3260–3264.
[15] S. Yin, W. Tu, Y. Sheng, Y. Du, M. Kraft, A. Borgna, R. Xu, *Adv. Mater.* **2018**, *30*, 1705106.
[16] a) L. Wei, W. Haije, N. Kumar, J. Peltonen, M. Peurla, H. Grenman, W. de Jong, *Catal. Today* **2021**, *362*, 35–46; b) M. Su, C. He, K. Shih, *Ceram. Int.* **2016**, *42*, 14793–14804; c) D. Zhou, Z. Cai, Y. Bi, W. Tian, M. Luo, Q. Zhang, Q. Zhang, Q. Xie, J. Wang, Y. Li, Y. Kuang, X. Duan, M. Bajdich, S. Siahrostami, X. Sun, *Nano Res.* **2018**, *11*, 1358–1368; d) Z. N. Zahran, E. A. Mohamed, T. Katsuki, Y. Tsubonouchi, M. Yagi, *ACS Appl. Energ. Mater.* **2022**, *5*, 1894–1904.
[17] P. F. Petrucci, M. E. Orsini, S. De Santis, G. Sotgiu, *Materials* **2022**.
[18] C. Rincke, S. Bette, R. E. Dinnebier, W. Voigt, *Eur. J. Inorg. Chem.* **2015**, *2015*, 5913–5920.
[19] a) M. Qayoom, R. Bhat, K. Asokan, M. A. Shah, G. N. Dar, *J. Mater. Sci. Mater. Electron.* **2020**, *31*, 8268–8282; b) B. S. Yadav, R. Singh, A. K. Vishwakarma, N. Kumar, *J. Supercond. Novel Magn.* **2020**, *33*, 2199–2208.
[20] A. M. Jubb, H. C. Allen, *ACS Appl. Mater. Interfaces* **2010**, *2*, 2804–2812.
[21] a) L. Yan, Y. Ren, J. Shen, H. Wang, J. Ning, Y. Zhong, Y. Hu, *Energy Technol.* **2020**, *8*, 2000607; b) N. Buzgar, A. I. Apopei, (Ed.: D. o. G. University of Iaşi, Romania), **2009**.
[22] R. A. Nyquist, C. L. Putzig, R. O. Kagel, M. A. Leugers, *Handbook of Infrared and Raman Spectra of Inorganic Compounds and Organic Salts: Infrared Spectra of Inorganic Compounds*, Elsevier Science, **1971**.
[23] Y. Gu, D.-H. Park, M.-H. Kim, J.-H. Byeon, D.-M. Lim, S.-H. Park, J.-H. Kim, J.-S. Jang, K.-W. Park, *Chem. Eng. J.* **2024**, *480*, 147789.
[24] a) C. Andronescu, S. Barwe, E. Ventosa, J. Masa, E. Vasile, B. Konkena, S. Möller, W. Schuhmann, *Angew. Chem. Int. Ed.* **2017**, *56*, 11258–11262; b) A. P. Grosvenor, M. C. Biesinger, R. S. C. Smart, N. S. McIntyre, *Surf. Sci.* **2006**, *600*, 1771–1779.
[25] M. C. Biesinger, B. P. Payne, A. P. Grosvenor, L. W. M. Lau, A. R. Gerson, R. S. C. Smart, *Appl. Surf. Sci.* **2011**, *257*, 2717–2730.
[26] I. J. Godwin, M. E. G. Lyons, *Electrochem. Commun.* **2013**, *32*, 39–42.
[27] T. Shinagawa, A. T. Garcia-Esparza, K. Takanabe, *Sci. Rep.* **2015**, *5*, 13801.
[28] R. L. Doyle, I. J. Godwin, M. P. Brandon, M. E. G. Lyons, *Phys. Chem. Chem. Phys.* **2013**, *15*, 13737–13783.
[29] K. Ishikawa, T. Yoshioka, T. Sato, A. Okuwaki, *Hydrometallurgy* **1997**, *45*, 129–135.
[30] a) Y. Sugawara, K. Kamata, E. Hayashi, M. Itoh, Y. Hamasaki, T. Yamaguchi, *ChemElectroChem* **2021**, *8*, 4392–4392; b) H. Bandal, K. K. Reddy, A. Chaugule, H. Kim, *J. Power Sources* **2018**, *395*, 106–127.

Manuscript received: February 14, 2024
Revised manuscript received: May 14, 2024